

GW effects on the topology of type-II Dirac cones in NiTe₂, PtSe₂ and PtTe₂

Franz Fischer,^{1,2} Abderrezak Torche,¹ Marta Prada,^{3,1} and Gabriel Bester^{1,4}

¹*Physical Chemistry and Physics Departments, University of Hamburg, Hamburg 22761, Germany*

²*Max Planck Institute for the Structure and Dynamics of Matter, 22761 Hamburg, Germany*

³*Institute for Theoretical Physics, University of Hamburg, Hamburg 22761, Germany*

⁴*The Hamburg Centre for Ultrafast Imaging, Luruper Chaussee 149, 22761 Hamburg, Germany.*

Many-body correlations are known to be responsible for a broad range of fascinating physical phenomena, introducing corrections that appear elusive at the single-particle level. An example of this is the Lifshitz transition that occurs as the Fermi surface topology changes when *e.g.* Coulomb interaction effects break into the picture. In particular, the Fermi velocity renormalization can lead a type-II Weyl semimetal at mean-field level to become a trivial or a type-I Dirac material when correlations are accounted for, which is far from being obvious. In this work we scrutinize the band structure of NiTe₂, a material that features a type-II Dirac point near the Fermi level within the mean-field approach. Including GW-level correlations, our findings showcase anisotropic corrections on the Dirac carrier velocity exceeding 100 % enhancements, underscoring the nuanced influence of electronic interactions in the band structure. We also consider type-II Dirac crossings in PtSe₂ and PtTe₂ and observe that including many-body effects via GW the band topology changes, featuring trivial topology and type-I Dirac crossings, respectively. Our findings highlights the necessity to evaluate the many-body effects on non-trivial bands, contributing essential insights to the broader exploration of many-body correlation effects in type-II Dirac points of condensed-matter systems.

I. INTRODUCTION

The rise of graphene in 2004 [1, 2] and the subsequent discovery of topological insulators [3] have brought the study of Dirac materials to the forefront of contemporary research [4, 5]. The insulating character of the bulk with intriguing conducting edges led to a whole new paradigm of novel states of matter that are mostly probed in transport, magnetic and thermodynamic experiments [5]. Recently, a new class of materials has been found within this family, namely the so-called type-II Dirac materials [6]. Whereas in type-I structures the Fermi surface can be reduced to a point, type-II Dirac fermions show an overtilted conic dispersion, such that the Fermi surface (FS) forms an open arc where electron and hole pockets touch when plotted in two dimensions (see Fig. 1). This Fermi arc indicate the presence of surface states in the material with exceptional properties. The nontrivial topology involves the presence of topologically protected surface states and bulk band crossings, giving rise to interesting phenomena that can be exploited for novel electronic and spintronic devices: The anisotropic chiral anomaly [7], unusual magnetoresistance with Landau level collapse [8] and novel quantum oscillations [9] are a few examples. From a high-energy physics perspective, as type-II Dirac electrons violate Lorentz invariance, it has been suggested that the low-energy excitations of these Dirac materials present a parallelism with those of quantum field theories of curved spaces [10].

Type-II Dirac materials are nowadays a fast-growing family that includes many transition metal dichalcogenides (TMDs) (WTe₂, NiTe₂, PtTe₂, PtSe₂) [6, 11, 12], transition metal icosagenides: MA₃ (M=V, Nb, Ta and A=Al, Ga, In) [13] and some Full-Heusler compounds XMg₂Ag (with X=Pr, Nd, Sm) [14]. NiTe₂ stands out among these materials, as the Dirac point

(DP) lies in close vicinity of the Fermi level [15]. For all the previous materials, *ab-initio* density-functional theory (DFT) calculations confirm the type-II character. However, the group velocity that determines the classification of the Dirac point is renormalized when many-body effects are included [5, 16–18]. As encountered by Kotov *et al.* [16] and by Trevisanutto *et al.* [17], the enhancement of the electronic correlation near the weakly screened carriers at the Fermi level in graphene leads to an isotropic renormalization of the Fermi velocity by 17% at the GW level, in better agreement with the experiment [19]. In type-II Dirac materials the situation is different: being highly anisotropic, we expect many-body corrections to deform the Dirac cones, which can lead to a change in the topology if correlation effects are strong enough, as recently observed by Beau *et al.* in T_d-MoTe₂ with ultrafast laser pulses [20]. Namely, a renormalization of the electronic band structure due to dynamical changes in the effective electronic correlations caused a transient change of the spectral weight on the Fermi surface, yielding a Lifshitz transition.

The purpose of the present work is to examine the many-body effects on the band dispersion and topology of commonly studied type-II materials: NiTe₂, PtSe₂ and PtTe₂. This has been achieved by calculating the *ab-initio* electron self-energy at the GW level [21]. We find that many-body effects have a tendency to tilt the NiTe₂ Dirac cone towards the type-I situation, with an enhanced and highly anisotropic Dirac fermion velocity (v_{DF}) renormalization. Although the induced tilt is not large enough to induce a topological transition in NiTe₂, we observe change in the band orderings in PtSe₂ and PtTe₂, indicating a fundamental change in the topology as correlations are included. This work underscores the importance of correlated effects on the band topology, mainly due to the effects of the *d*-bands, which is far

from being obvious *a priori*.

II. TYPE-II DIRAC POINTS AND COMPUTATIONAL METHODS

Whereas type-I Dirac fermions present a point-like Fermi surface, type-II Dirac fermions emerge at the boundary between electron and hole pockets, commonly termed as Fermi arc [see dark lines of Fig. 1 (right)]. This represents a novel type of fermion that breaks Lorentz invariance due to the over-tilting of the Dirac cone [6], yielding physical properties that are very different from those of type-I Dirac electrons. In particular, some TMDs feature type-II three-dimensional bulk Dirac fermions as a general consequence of a trigonal crystal field within the chalcogen p -orbitals [22]. Namely, a band-inversion on the main rotations along the growth direction k_z results in symmetry-protected crossings of the A_1 (p_z -orbital) and E -derived bands (p_x and p_y), which are split by a crystal field at Γ [22]. These bands behave differently under the three-fold rotations $C_{3\nu}$, protecting the crossing against hybridization, which is ensured along the $\Gamma \rightarrow A$ direction.

As stated by Soluyanov *et al.* [6], the most general Hamiltonian describing Weyl and DPs has the form:

$$H(\mathbf{k}) = \sum_{ij} k_i A_{ij} \sigma_j, \quad (1)$$

where A_{ij} is a generic 3×4 coefficient matrix with indices $i = x, y, z$ and $j = 0, x, y, z$ and σ_j corresponds to the 2×2 identity matrix ($j = 0$) or the Pauli matrices ($j = x, y, z$). Using that $\sigma_j^2 = \sigma_0$, the spin-degenerate eigenvalue spectrum is trivially given by:

$$\begin{aligned} \epsilon_{\pm}(\mathbf{k}) &= \sum_i k_i A_{i0} \pm \sqrt{\sum_j \left(\sum_i k_i A_{ij} \right)^2} \\ &= T(\mathbf{k}) \pm U(\mathbf{k}). \end{aligned} \quad (2)$$

The first term on the right-hand side can be considered the kinetic contribution $T(\mathbf{k})$, whereas the second one involves internal degrees of freedom and hence, takes the role of the potential component $U(\mathbf{k})$. It is the former term that induces the tilting of the Dirac dispersion. Whenever the ratio $|R(\mathbf{k})| = |T(\mathbf{k})/U(\mathbf{k})|$ is larger than one for a given \mathbf{k} direction, the Dirac cone is of type-II, as the tilt becomes large enough to cause contact between the open electron and hole pockets, in contrast to standard point-like Dirac touching (see Fig. 1).

In Ref. [6] a fit has been used to deduce the value of aforementioned ratio. We evaluate R using:

$$R(\mathbf{k}) = \frac{\epsilon_+(\mathbf{k}) + \epsilon_-(\mathbf{k})}{\epsilon_+(\mathbf{k}) - \epsilon_-(\mathbf{k})}, \quad (3)$$

showing that the dispersions of the upper and lower bands are sufficient for R , eliminating the need for low-energy Hamiltonian fitting. Note that (3) is sensitive to

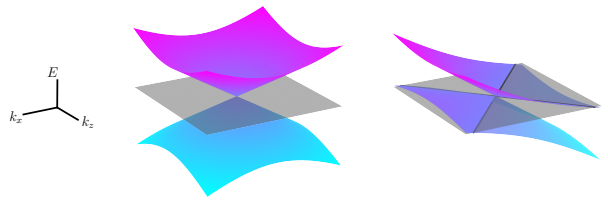


FIG. 1. In a type-I Dirac cone (left) the Fermi surface can be reduced to a point, whereas in a type II (right) the boundary between electron and hole pockets describes an open curve.

a rigid shift of the bands, making it necessary to set the zero-energy level to the DP.

To obtain the band structure, we perform a ground state calculation using DFT with norm-conserving, fully-relativistic pseudopotentials in the PBE parameterization from the PseudoDojo library [23], using the Quantum Espresso package [24]. The relaxation of the unit cell was performed until atomic forces are less than 10^{-3} Ry/Bohr. We then perform single-shot many-body calculations within the GW approximation using the Yambo package [25], which employs the Kohn-Sham energies and wave functions from the previous ground state calculation as input to generate the corrected quasiparticle energies and amplitudes. Both the plasmon pole approximation and real frequency integration methods are used to evaluate the self-energy. Employing the quasiparticle energies and the Wannier-orbitals from the ground state calculation, an effective many-body Hamiltonian is then generated with the wannier90 package [26]. This Hamiltonian is then used to generate the quasiparticle energies in any region of the Brillouin zone (BZ) and for any band in an accurate way via the Wannier interpolation. A cutoff of 30 Ha was needed to converge ground state properties such as the total energy and the Fermi level within the range of one meV. However, for the subsequent GW calculation, a cutoff of 60 Ha and k-mesh of $14 \times 14 \times 8$ were necessary to achieve convergence due to the presence of localized d -orbitals. For the screening computation, convergence has been achieved using 600 empty bands in the RPA formulation. A screening cutoff as high as 11 Ha was needed to converge the quasiparticle energies and the Fermi level.

III. RESULTS AND DISCUSSION

NiTe₂ crystallizes in the standard layered hexagonal structure of TMDs with 12 symmetry operations including inversion symmetry (space group 164). As a result, NiTe₂ possesses two symmetry-related type-II DPs along the $\Gamma \rightarrow A$ path located at $(0, 0, \pm Q)$ [27–29]. Namely, the crossing bands E (p_x, p_y) and A_1 (p_z) present opposite rotation character, preventing hy-

bridization and resulting in quadruply degenerate type-II DP [11, 12, 22, 28, 30].

In order to verify the existence of the type-II DP, we first employ a Löwdin population analysis within the **Quantum Espresso** package to project the wave functions onto atomic orbitals [24]. We utilize scalar-relativistic pseudopotentials and, in a first step, neglect spin-orbit interaction to preserve L and S as good quantum numbers and find that the major contribution of the crossing bands stems from the p -orbitals of the Te atoms. The splitting between the E (p_x - and p_y -orbitals) and A_1 bands (p_z -orbitals) is a consequence of the crystal field splitting (CFS), which is inverted along the $\Gamma \rightarrow A$ path. The type-II DP occurs when the CFS and the bandwidth of the dispersive p_z -orbitals have suitable magnitudes. Fig. 2 shows the contribution of the p_z -orbital (blue, A_1 anti-bonding band) and $p_{x,y}$ ones (orange, E bonding and anti-bonding) with (a) and without spin orbit coupling (SOC) (b), where the E manifold splits further into doublets. We observe a CFS of about 1.46 eV at Γ , whereas SOC is of the order of 360 meV (see double-headed arrows), where the latter is responsible for the splitting of the blue colored bands. The crossings are protected by symmetry, as the involved bands transform differently under rotations [22]. As shown in Fig. 2 (b) DP_1 results from the crossing of $|j = 1/2, |m_j| = 1/2\rangle$ (original E band) and the upper split-off band $|j = 3/2, |m_j| = 3/2\rangle$, composed mainly of the in-plane p -orbitals. On the other hand, the lower SOC split-off band $|j = 3/2, |m_j| = 1/2\rangle$ mixes with the $|j = 1/2, |m_j| = 1/2\rangle$ band, featuring an inverted band gap (IBG), where the band character flips on either side of the avoided crossing. Note that DFT calculations using SOC and spin polarization confirms the non-magnetic ground state of $NiTe_2$ despite the presence of Ni, rendering spin polarization unnecessary.

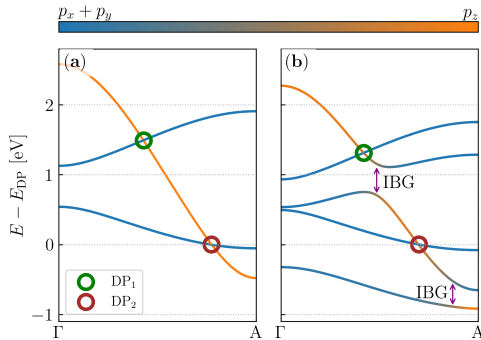


FIG. 2. Projection of the A_1 and E bands onto the Tellurium p -orbitals of $NiTe_2$, showing the p_z -orbital contributions (blue) and $p_{x,y}$ (orange) without SOC (a) and with SOC (b). DP_1 and DP_2 label the protected-by-symmetry crossings. Two IBGs are observed in (b), owing to SOC mixing. The DP_2 serves as the reference or zero-energy level.

We stress that we employ the DP energy as the reference energy, allowing a better visualization of the Dirac carrier velocity correction, which is the focus of this work.

Note that existing calculations yield the location of the DP with respect to the Fermi level at different positions: Ghosh *et al.* yield a DP 20 meV above the Fermi level [27], Mukherjee *et al.* encounter a DP 76 meV above the Fermi level [28], comparable to the value reported by Karn *et al.* [31], whereas Nurmamat *et al.* report this crossing 150 meV below Fermi energy [29]. The discrepancy is due to the starting functionals of the DFT calculations and to the high sensitivity of the DP position to small variations of structural parameters. Our initial DFT computation with relaxed cell parameters yielded a DP 50 meV above the PBE Fermi level, while it appears 0.61 eV below the Fermi energy employing G_0W_0 .

Once we have confirmed a type-II DP, we include the correlations via GW calculation at the single shot (G_0W_0). The CFS and band splitting are renormalized by many-body effects, and hence, the preservation of the topology cannot be guaranteed. Fig. 3 shows the band structures obtained with DFT (a) and G_0W_0 (b), allowing for a direct comparison. The band structure features

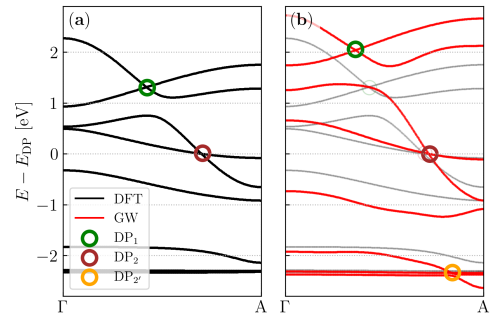


FIG. 3. Band structure for $NiTe_2$ along the $\Gamma \rightarrow A$ direction employing DFT (a) and GW (b). The DFT results are overlaid with the GW results for direct comparison. The band structure features a type-I DP (DP_1), two inverted bandgaps due to SOC and a type-II DP (DP_2). The DP_2 serves as the reference or zero-energy level.

a type-I and a type-II DP (green and brown circles in Fig. 3, respectively) and two IBGs. The GW correction enhances the effect of the localized d -orbitals, which can potentially modify the band ordering. To illustrate this, we include the orbital projections of the different bands in Fig. 4. As we can appreciate, the top five bands correspond to the p -orbitals of both Te atoms (see also the top row of Fig. 5), where the absolute orbital projections are displayed. Band ordering and topology are preserved on these top bands both at the DFT and GW level, showing the original type-I and type-II DP. However, the two lower d -bands that show no crossings using DFT, feature a band crossing ($DP_{2'}$) when including the GW corrections, signaling that the band topology could be affected as the electronic correlations are accounted for.

It is generally accepted that the Fermi level calculation within GW is cumbersome, as it requires corrections of the whole valence bands manifold, including deep and

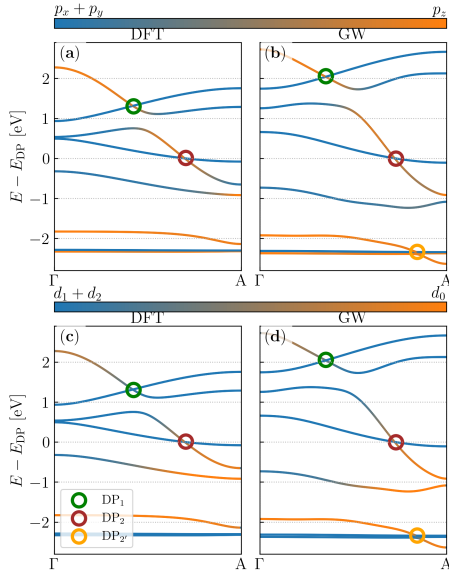


FIG. 4. Normalized relative orbital projections of the p -orbitals in (a,b) and d -orbitals in (c,d) comparing DFT and GW results along the $\Gamma \rightarrow A$ path for NiTe₂, respectively. The color indicates the relative weight of the contributions as labeled above. The circles indicate the type I (green) and type-II (brown, orange) DPs, respectively. For more details, see Fig. 5)

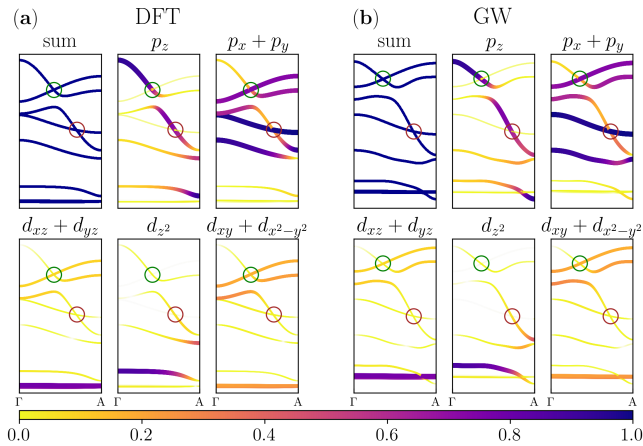


FIG. 5. Normalized absolute projections of the p -orbitals (upper panels) and d -orbitals (lower panels) comparing DFT (a) and GW (b) results along the $\Gamma \rightarrow A$ path for NiTe₂, respectively. The color and size indicates the relative weight of the contributions as labeled above. The circles indicate the type I (green) and type-II (brown, orange) DPs, respectively. The individual panels focus on the orbitals labeled above.

very localized levels. The plasmon pole approximation used in this work is particularly known to be more challenging for the deep and localized states. Note that our DFT in-plane cell parameters are in very good agreement with experiments [32] with less than 0.01 % discrepancy, whereas our out-of-plane crystal axis is, however, 1.25 %

shorter than the experimental one (see table I). As Ferreira *et al.* [33], pointed out, the DP₂ energy shifts by a few hundred meV when the unit cell is strained. We indeed observed a shift of the DP₂ to 300 meV below the Fermi level by performing G_0W_0 calculations using the experimental c -axis length instead of the relaxed DFT value. This sets the DP just about 150 meV below the experimentally obtained value [29]. Moreover, the Fermi velocity renormalization and band topology were insensitive to the cell parameters.

TABLE I. Experimental versus DFT cell parameters for NiTe₂: lattice constant in-plane (a) and out-of-plane (c), both in Å.

	a	c
PBE	3.854	5.197
Exp. [32]	3.858	5.264

We examine the real frequency integration of the self-energy as implemented in the *Yambo* package. In particular, the zero-momentum limit of the electron energy loss spectrum, E_{LS} give access to the dynamical behavior of the dielectric function $\epsilon^{-1}(q \simeq 0, \omega)$, namely,

$$E_{LS}(q \simeq 0, \omega) = -\Im[\epsilon^{-1}(q \simeq 0, \omega)].$$

Peaks of $E_{LS}(q \simeq 0, \omega)$ are related to plasmon resonances where $|\epsilon(q \simeq 0, \omega)| = 0$. We indeed observe a single pole in ϵ^{-1} in the frequency domain, indicating the validity of the single plasmon pole approach. It is worth noting that the z -renormalization factor in our G_0W_0 calculation is close to 1 ($z \approx 0.8$) indicating a low sensitivity of the GW calculation to the starting DFT computation. These observations discard the possibility that the starting exchange-correlation functionals are responsible for overshooting the Fermi level. In order to capture the

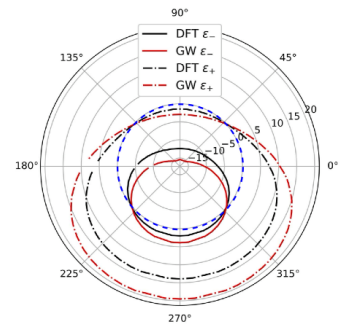


FIG. 6. Polar plot showing v_{DF} for the ϵ_{\pm} bands forming the DP₂ cone, where 0° is chosen to be the x -axis (blue dashed circle corresponds to zero v_{DF}). The radial component is in units of 10^6 m/s. The black curves correspond to DFT results, whereas the red ones correspond to the GW calculation. The dashed and solid curves correspond to the upper and lower bands, respectively.

velocity renormalization anisotropy of the type-II DP, we

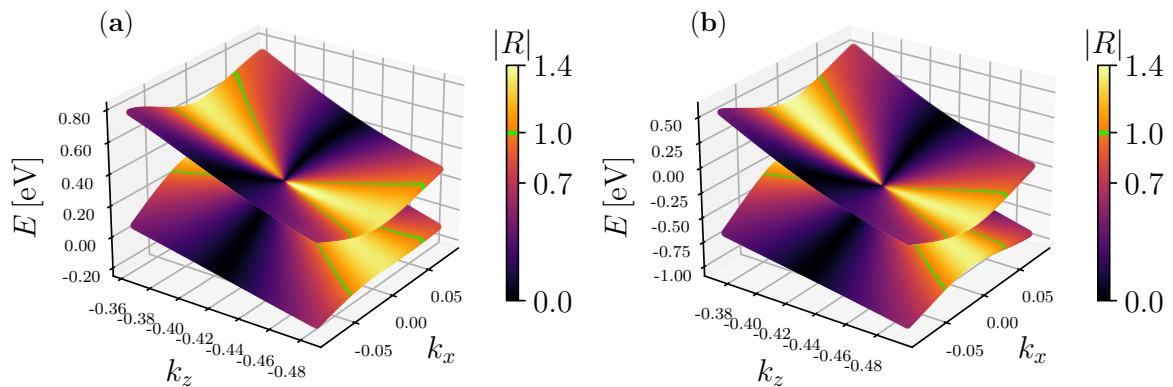


FIG. 7. The ϵ_{\pm} band dispersion of NiTe₂, forming the type-II Dirac point (DP₂), is visualized in 3D within the xz -plane for both (a) DFT and (b) GW computations. The color bar indicates the absolute value of the R ratio (see main text). The Fermi level in the DFT results is set to zero, while the zero-energy reference for the GW energies is shifted to the DP₂ energy.

show in Fig. 6 (a) a polar plot where the radial part indicates the Dirac fermion velocity v_{DF} (in units of 10^6 m/s) and the angle θ denotes the direction within the xz -plane, where we chose 0° and 90° to be the x - and z -directions, respectively. We focus on the xz -plane, as the yz -plane can be obtained by symmetry. The black curves correspond to DFT results, whereas the red ones correspond to the GW calculation. Solid and dashed curves correspond to ϵ_- and ϵ_+ , respectively.

We notice sign changes of ϵ_- at $-\frac{\pi}{2} \pm \frac{\pi}{4}$ and ϵ_+ at $\frac{\pi}{2} \pm \frac{\pi}{4}$, which is consistent with the type-II Dirac cone (see Fig. 1). This change of sign offers thus a straightforward manner to distinguish between type-I and type-II Dirac cones. We observe that, unlike along z , v_{DF} is symmetric along the x -direction, which is inherited from the unit cell structure. v_{DF} varies between -15 and 20×10^6 m/s, that is, the carriers are faster than in graphene for some directions in reciprocal space [34]. The GW renormalization of v_{DF} is highly anisotropic and varies between 25% and 115%. This renormalization is relatively large compared to the isotropic correction of 17% in graphene [16, 17]. This is surprising, as the reduced dimensionality of graphene makes the screening relatively weak (i.e., enhanced electron correlations), as compared to the 3D bulk structure of NiTe₂. However, as stated in Ref. [28] the d -orbitals play an important role in the band structure of NiTe₂, yielding important GW corrections. In our GW calculation, the influence of the d -orbitals is taken into account, as the convergence of the exchange component of the self-energy requires a relatively high cutoff (over 120 Ry). This is a clear indication of the presence of these localized d -orbitals with an important influence on the Dirac bands, causing a large GW correction. In particular, at the regions where v_{DF} is close to zero, correlation effects are enhanced due to localization in real space, yielding large relative corrections. This is evident in the region between $\theta_1 = \pi/4$ ($-\pi/4$) and $\theta_2 = 3\pi/4$ ($-3\pi/4$) for ϵ_+ (ϵ_-). It is worth noting that GW corrections preserve the directions where ϵ_{\pm} are zero, implying that the

topology remains intact, as will be discussed below.

Fig. 7 (a) and (b) show a 3D plot of the ϵ_{\pm} branches forming the type-II Dirac cone at both the DFT and GW level, where the color bar indicates the absolute value of the kinetic to potential energy ratio $R(\mathbf{k})$, as defined in Eq. (3). This has been achieved using the Wannier interpolation techniques, as implemented in the **wannier90** code [26] and the **WannierTools** code [35] on top of the DFT/GW bands. The existence of a region with $|R(\mathbf{k})| > 1$ is characteristic of a type-II Dirac cone [6], which is observed in the BZ region near the k_x axes (yellow). Within that region, either the upper band ϵ_+ (right side of DP) or the lower band ϵ_- (left side of DP) crosses the Fermi level. The Fermi arc, where v_{DF} vanishes, is highlighted with light green lines in Fig. 7. We note that the effect of the GW correction is to reduce the $|R(\mathbf{k})| > 1$ region, although no Lifshitz transition occurs.

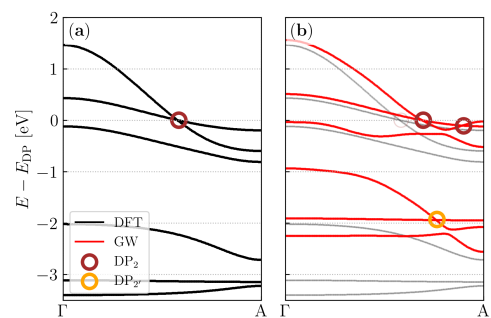


FIG. 8. Band structure for PtSe₂ along the $\Gamma \rightarrow A$ direction employing DFT (a) and GW (b). The DFT results are overlaid with the GW results for direct comparison. The type-II DPs are marked with brown and orange circles, respectively.

We further investigate the effect on other type-II Dirac materials, namely PtSe₂ and PtTe₂. We first compute the orbital projection on PtSe₂ along the $\Gamma \rightarrow A$ path in the absence of SOC and encounter a slightly different band ordering as compared to NiTe₂. Namely, the (anti-

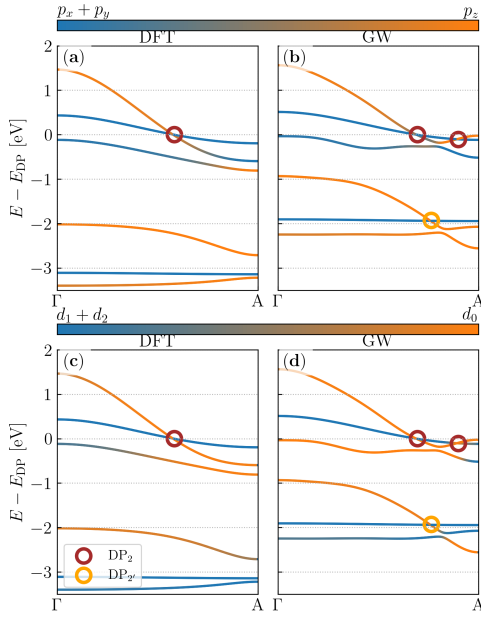


FIG. 9. Normalized relative orbital projections of the p -orbitals in (a,b) and d -orbitals in (c,d) comparing DFT and GW results along the $\Gamma \rightarrow A$ path for PtSe₂, respectively. The color indicates the relative weight of the contributions as labeled above. The circles indicate the type I (green) and type-II (brown, orange) DPs, respectively. For more details, see Fig. 10.

bonding) E band is above the A_1 band, which can only cross with the bonding E band as it disperses and the CFS is inverted. Note that the A_1 band is less dispersive compared to that of NiTe₂. This can be explained in terms of the smaller atomic radii of the chalcogen ($r_{\text{Se}} < r_{\text{Te}}$), which is responsible for the out-of-plane dispersion (weaker p_z bond), while the unit cell of both materials have comparable dimensions.

We then proceed as above and compute the band structure numerically. Fig. 8 shows the DFT results and GW corrections for PtSe₂. As the CFS at Γ and the bandwidth of E are within the same order of magnitude, we observe a smaller velocity renormalization. The DP₂ crossing is observed in the DFT calculation. Strikingly, we observe a change in the topology of the band structure as the GW corrections are included, featuring a double crossing, see Fig. 8 (b). This suggests a transition to a trivial metal topology as correlation effects are accounted for.

The orbital projections for both sets of results are illustrated in Fig. 9 and Fig. 10 (normalized and relative, respectively). At the DFT level (left panels), we observe that the CFS inversion is maintained. However, along the $\Gamma \rightarrow A$ path in the GW results, this inversion no longer occurs, indicating identical band ordering at Γ and A . Conversely, we observe a crossing in the lower-lying d -bands at the GW level, which is absent in the DFT calculation, signaling an inversion in the CFS of the d

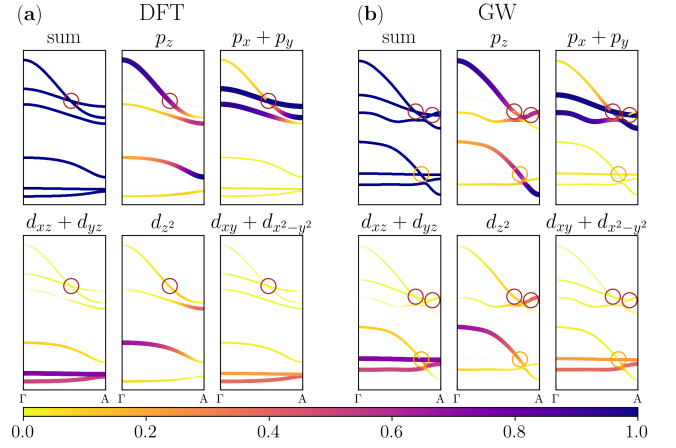


FIG. 10. Normalized absolute projections of the p -orbitals (upper panels) and d -orbitals (lower panels) comparing DFT (a) and GW (b) results along the $\Gamma \rightarrow A$ path for PtSe₂, respectively. The color and size indicates the relative weight of the contributions as labeled above. The circles indicate the type I (green) and type-II (brown, orange) DPs, respectively. The individual panels focus on the orbitals labeled above.

manifold.

We finally analyse PtTe₂. As Fig. 11 shows, PtTe₂ features a DP₁, IBG and DP₂ at the DFT level. The GW computation introduces a correction on the E bands, resulting in a symmetry switching or band reordering. We speculate that this is due to the larger contribution of the d -bands, however, the exact mechanism would involve a detailed analysis of the wavefunction which is beyond the scope of this work. As a result, we obtain two type-I DPs along the $\Gamma \rightarrow A$ direction, whereas the type-II DP is absent at the GW level.

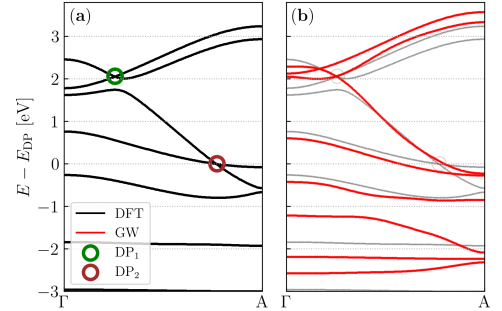


FIG. 11. Band structure for PtTe₂ along the $\Gamma \rightarrow A$ direction employing DFT (a) and GW (b). The DFT results are overlaid with the GW results for direct comparison. Type-I and type-II Dirac points are denoted by green and brown circles, respectively.

To enhance clarity of the discussion above, we include the orbital projections with both methods, as previously done for NiTe₂ and PtSe₂. It is worth noting that the DP₂ (DFT) is a few eV below the Fermi level, rendering this material less relevant as a topologically non-trivial

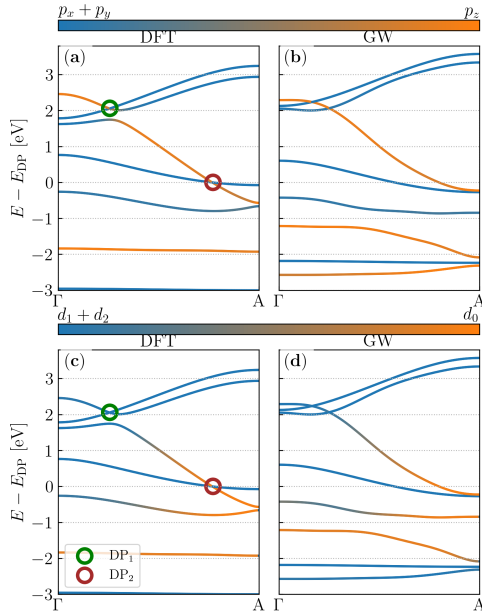


FIG. 12. Normalized orbital projections of the p -orbitals in (a,b) and d -orbitals in (c,d) comparing DFT and GW results along the $\Gamma \rightarrow A$ path for PtTe₂, respectively. The color indicates the relative weight of the contributions as labeled above. The circles indicate the type I (green) and type-II (brown, orange) DPs, respectively.

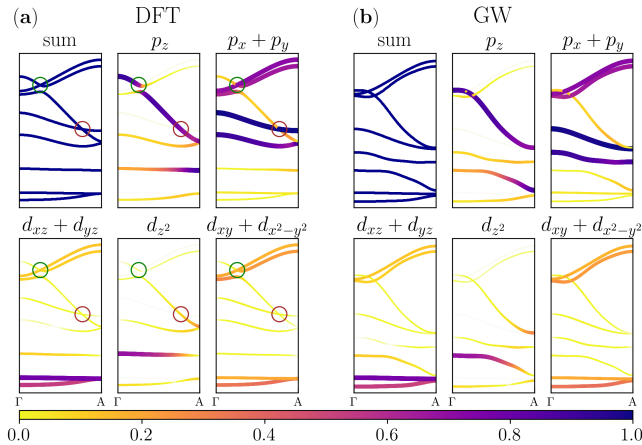


FIG. 13. Normalized orbital projections of the p -orbitals (upper panels) and d -orbitals (lower panels) comparing DFT (a) and GW (b) results along the $\Gamma \rightarrow A$ path for PtTe₂, respectively. The color and size indicates the relative weight of the contributions as labeled above. The circles indicate the type I (green) and type-II (brown, orange) DPs, respectively. The individual panels focus on the orbitals labeled above.

material, however, it underscores the nuanced influence of electronic interactions in the band structure of TMDs.

IV. CONCLUSIONS

In this work we have scrutinized on the effects of the GW-level many-body correlations on the band structure and topology of NiTe₂, PtSe₂ and PtTe₂. For the former we observe a significant renormalization of the Fermi velocity leading to a substantial tilt of the Dirac cone. We have also examined the impact of strain and found that using the compressed DFT-relaxed unit cell can cause a shift in the energetic position of the type-II DP at both the DFT and GW levels. In contrast, using the experimentally obtained lattice constant yields better agreement of the DP energy with experimental values. In spite of the corrections to the CFS and band bendings, the topology is preserved in NiTe₂ *i.e.*, it is a type-II Dirac materials both at the DFT and at the GW level. However, PtSe₂ becomes a trivial metal, featuring a crossing of d -character bands deep below the Fermi level. Finally, we examined PtTe₂ and observe a double type-I Dirac crossing, suggesting a symmetry switching as the GW corrections are introduced. These findings highlight the necessity to evaluate accurate computations, as it is not obvious *a priori*.

V. ACKNOWLEDGMENTS

This work is supported by the Cluster of Excellence 'The Hamburg Centre for Ultrafast Imaging' of the Deutsche Forschungsgemeinschaft (DFG) - EXC 1074 - project ID 194651731. Calculations were carried out on Hummel funded by the DFG - 498394658.

VI. REFERENCES

-
- [1] K. S. Novoselov, A. K. Geim, S. V. Morozov, D.-e. Jiang, Y. Zhang, S. V. Dubonos, I. V. Grigorieva, and A. A. Firsov, Electric field effect in atomically thin carbon films, *science* **306**, 666 (2004).
 - [2] A. K. Geim and K. S. Novoselov, The rise of graphene, in *Nanoscience and technology: a collection of reviews from nature journals* (World Scientific, 2010) pp. 11–19.

- [3] M. Z. Hasan and C. L. Kane, Colloquium: topological insulators, *Reviews of modern physics* **82**, 3045 (2010).
- [4] F. Giustino, J. H. Lee, F. Trier, M. Bibes, S. M. Winter, R. Valentí, Y.-W. Son, L. Taillefer, C. Heil, A. I. Figueroa, *et al.*, The 2021 quantum materials roadmap, *Journal of Physics: Materials* **3**, 042006 (2021).
- [5] T. O. Wehling, A. M. Black-Schaffer, and A. V. Balatsky, Dirac materials, *Advances in Physics* **63**, 1 (2014).
- [6] A. A. Soluyanov, D. Gresch, Z. Wang, Q. Wu, M. Troyer, X. Dai, and B. A. Bernevig, Type-II Weyl semimetals, *Nature* **527**, 495 (2015).
- [7] M. Udagawa and E. J. Bergholtz, Field-selective anomaly and chiral mode reversal in type-II Weyl materials, *Physical review letters* **117**, 086401 (2016).
- [8] Z.-M. Yu, Y. Yao, and S. A. Yang, Predicted unusual magnetoresponse in type-II Weyl semimetals, *Physical review letters* **117**, 077202 (2016).
- [9] T. O'Brien, M. Diez, and C. Beenakker, Magnetic breakdown and klein tunneling in a type-II Weyl semimetal, *Physical review letters* **116**, 236401 (2016).
- [10] G. E. Volovik, Black hole and hawking radiation by type-II Weyl fermions, *JETP letters* **104**, 645 (2016).
- [11] H. Huang, S. Zhou, and W. Duan, Type-II Dirac fermions in the PtSe₂ class of transition metal dichalcogenides, *Physical Review B* **94**, 121117 (2016).
- [12] M. Yan, H. Huang, K. Zhang, E. Wang, W. Yao, K. Deng, G. Wan, H. Zhang, M. Arita, H. Yang, *et al.*, Lorentz-violating type-II Dirac fermions in transition metal dichalcogenide PtTe₂, *Nature communications* **8**, 1 (2017).
- [13] T.-R. Chang, S.-Y. Xu, D. S. Sanchez, W.-F. Tsai, S.-M. Huang, G. Chang, C.-H. Hsu, G. Bian, I. Belopolski, Z.-M. Yu, *et al.*, Type-ii symmetry-protected topological dirac semimetals, *Physical review letters* **119**, 026404 (2017).
- [14] W. Meng, X. Zhang, Y. Liu, X. Dai, and G. Liu, Lorentz-violating type-ii dirac fermions in full-heusler compounds xmg₂ag (x= pr, nd, sm), *New Journal of Physics* **22**, 073061 (2020).
- [15] C. Xu, B. Li, W. Jiao, W. Zhou, B. Qian, R. Sankar, N. D. Zhigadlo, Y. Qi, D. Qian, F.-C. Chou, *et al.*, Topological type-II Dirac fermions approaching the fermi level in a transition metal dichalcogenide NiTe₂, *Chemistry of materials* **30**, 4823 (2018).
- [16] V. N. Kotov, B. Uchoa, V. M. Pereira, F. Guinea, and A. C. Neto, Electron-electron interactions in graphene: Current status and perspectives, *Reviews of Modern Physics* **84**, 1067 (2012).
- [17] P. E. Trevisanutto, C. Giorgetti, L. Reining, M. Ladisa, and V. Olevano, *Ab-Initio* G-W many-body effects in graphene, *Physical review letters* **101**, 226405 (2008).
- [18] S. Banerjee, D. S. Abergel, H. Ågren, G. Aeppli, and A. V. Balatsky, Interacting Dirac materials, *Journal of Physics: Condensed Matter* **32**, 405603 (2020).
- [19] A. Bostwick, T. Ohta, T. Seyller, and E. Horn K Rotenberg, Quasiparticle dynamics in graphene, *Nature Physics* **3**, 36 (2007).
- [20] S. Beaulieu, S. Dong, N. Tancogne-Dejean, M. Dendzik, T. Pincelli, J. Maklar, R. P. Xian, M. A. Sentef, M. Wolf, A. Rubio, *et al.*, Ultrafast dynamical Lifshitz transition, *Science Advances* **7**, eabd9275 (2021).
- [21] L. Hedin, New method for calculating the one-particle Green's function with application to the electron-gas problem, *Physical Review* **139**, A796 (1965).
- [22] M. Bahramy, O. Clark, B.-J. Yang, J. Feng, L. Bawden, J. Riley, I. Marković, F. Mazzola, V. Sunko, D. Biswas, *et al.*, Ubiquitous formation of bulk Dirac cones and topological surface states from a single orbital manifold in transition-metal dichalcogenides, *Nature materials* **17**, 21 (2018).
- [23] M. Van Setten, M. Giantomassi, E. Bousquet, M. J. Verstraete, D. R. Hamann, X. Gonze, and G.-M. Rignanese, The pseudodojo: Training and grading a 85 element optimized norm-conserving pseudopotential table, *Computer Physics Communications* **226**, 39 (2018).
- [24] P. Giannozzi, O. Andreussi, T. Brumme, O. Bunau, M. B. Nardelli, M. Calandra, R. Car, C. Cavazzoni, D. Ceresoli, M. Cococcioni, *et al.*, Advanced capabilities for materials modelling with quantum espresso, *Journal of physics: Condensed matter* **29**, 465901 (2017).
- [25] D. Sangalli, A. Ferretti, H. Miranda, C. Attaccalite, I. Marri, E. Cannuccia, P. Melo, M. Marsili, F. Paleari, A. Marrazzo, *et al.*, Many-body perturbation theory calculations using the yambo code, *Journal of Physics: Condensed Matter* **31**, 325902 (2019).
- [26] G. Pizzi, V. Vitale, R. Arita, S. Blügel, F. Freimuth, G. Géranton, M. Gibertini, D. Gresch, C. Johnson, T. Koretsune, J. Ibañez-Azpiroz, H. Lee, J.-M. Lihm, D. Marchand, A. Marrazzo, Y. Mokrousov, J. I. Mustafa, Y. Nohara, Y. Nomura, L. Paulatto, S. Poncé, T. Ponweiser, J. Qiao, F. Thöle, S. S. Tsirkin, M. Wierzbowska, N. Marzari, D. Vanderbilt, I. Souza, A. A. Mostofi, and J. R. Yates, Wannier90 as a community code: new features and applications, *Journal of Physics: Condensed Matter* **32**, 165902 (2020).
- [27] B. Ghosh, D. Mondal, C.-N. Kuo, C. S. Lue, J. Nayak, J. Fujii, I. Vobornik, A. Politano, and A. Agarwal, Observation of bulk states and spin-polarized topological surface states in transition metal dichalcogenide Dirac semimetal candidate NiTe₂, *Physical Review B* **100**, 195134 (2019).
- [28] S. Mukherjee, S. W. Jung, S. F. Weber, C. Xu, D. Qian, X. Xu, P. K. Biswas, T. K. Kim, L. C. Chapon, M. D. Watson, *et al.*, Fermi-crossing type-II Dirac fermions and topological surface states in NiTe₂, *Scientific reports* **10**, 1 (2020).
- [29] M. Nurmamat, S. V. Ereemeev, X. Wang, T. Yoshikawa, T. Kono, M. Kakoki, T. Muro, Q. Jiang, Z. Sun, M. Ye, *et al.*, Bulk Dirac cone and highly anisotropic electronic structure of NiTe₂, *Physical Review B* **104**, 155133 (2021).
- [30] O. J. Clark, F. Mazzola, I. Marković, J. M. Riley, J. Feng, B. Yang, K. Sumida, T. Okuda, J. Fujii, I. Vobornik, *et al.*, A general route to form topologically-protected surface and bulk Dirac fermions along high-symmetry lines, *Electronic Structure* **1**, 014002 (2019).
- [31] N. Karn and V. Awana, Band topology and non-trivial surface states in type-ii dirac semimetal x(ni, pd)te₂, *Materials Today: Proceedings* <https://doi.org/10.1016/j.matpr.2023.05.202> (2023).
- [32] J. F. H. L. Monteiro, M. B. Marciniak, A. R. Jurelo, E. C. Siqueira, F. T. Dias, and J. L. P. Júnior, Synthesis and microstructure of NiTe₂, *Journal of Crystal Growth* **478**, 129 (2017).
- [33] P. P. Ferreira, A. L. Manesco, T. T. Dorini, L. E. Correa, G. Weber, A. J. Machado, and L. T. Eleno, Strain engineering the topological type-II Dirac semimetal NiTe₂, *Physical Review B* **103**, 125134 (2021).

- [34] D. C. Elias, R. V. Gorbachev, A. S. Mayorov, S. V. Morozov, A. A. Zhukov, P. Blake, L. A. Ponomarenko, I. V. Grigorieva, K. S. Novoselov, F. Guinea, and A. K. Geim, Dirac cones reshaped by interaction effects in suspended graphene, *Nature Physics* **7**, 701–704 (2011).
- [35] Q. Wu, S. Zhang, H.-F. Song, M. Troyer, and A. A. Soluyanov, Wanniertools : An open-source software package for novel topological materials, *Computer Physics Communications* **224**, 405 (2018).